RSC Advances

PAPER

View Article Online
View Journal | View Issue

Cite this: *RSC Adv.*, 2025, **15**, 27526

Encapsulation of nanoparticles with Xe adsorption sites into MOFs for enhanced Xe/Kr separation

Chunhui Wu, *[ab] He Zhou,[a] Xiaoling Wu, [ab] Huimin Xu,[a] Youshi Zeng,[a] Xinxin Chu*[a] and Wei Liu[ab]

Received 14th May 2025
Accepted 21st July 2025

DOI: 10.1039/d5ra03389f

rsc.li/rsc-advances

Xenon (Xe) and krypton (Kr) are important gases with significant industrial and medical applications. Metal–organic frameworks (MOFs) are a promising class of sorbent materials for Xe/Kr separation. To enhance the Xe/Kr separation performance of MOFs, we develop a strategy to encapsulate Pt nanoparticles into MOFs to introduce strong Xe adsorption sites. Xe and Kr adsorption and separation studies show that Pt@UiO-66 exhibits 21% higher Xe uptake capacity and a 7% increase in Xe/Kr selectivity compared to UiO-66 due to the introduced Xe adsorption sites, despite the Brunauer–Emmett–Teller (BET) surface area decreasing. These findings have led to an 88% extension of column breakthrough time during Xe/Kr separation under identical conditions. We further demonstrate that this approach can be extended to other MOFs with potential for Xe/Kr separation.

Introduction

Xenon (Xe) and krypton (Kr) are noble gases that are used in various applications and fields, such as in medicine and as lighting for transport systems, *etc.* Xe can be used for flash lamps, arc lamps, imaging, neuroprotection, anaesthesia, and radiation detection.[1–3] Kr is also widely used in magnetic resonance imaging, photographic flashes and fluorescent lamps.[4–6] Xe and Kr mixtures can be sourced from air as a by-product of oxygen production. Currently, cryogenic distillation is mainly used for the separation of Kr and Xe from the atmosphere and spent nuclear fuel.[7–9] However, this process is capital and energy intensive.[10] Recently, a number of studies have shown that physical adsorption using porous materials for rare gas separation is an energy efficient and environmentally friendly process.[11–14]

Like traditional porous materials such as activated carbon and zeolites, metal–organic frameworks (MOFs) have been widely applied in gas separation and capture due to their high specific surface area, regular and adjustable pore structure, and structural diversity.[15–24] MOFs also show excellent separation performance for Xe and Kr.[25–31] Given the extremely low concentration of Xe and Kr in gas streams and their inert and weak interaction properties, a adsorption material must have optimal adsorption capacity and selectivity to make the process economically viable. Some previous work has shown that the introduction of small amounts of noble metal nanoparticles into porous materials can greatly enhance the adsorptive separation of gases.[32–35] For example, Qiang Xu and co-workers demonstrated that the uniform dispersion of bimetallic Au–Pd nanoparticles in MOFs is the key for improved adsorption of hydrogen.[36] Recently, a density-functional theory (DFT) study on the binding between Xe and metal nanoparticles (NPs) (such as Pt, Pd, Cu and Ag) suggested the existence of a strong interaction between xenon and the nanoparticles.[37,38]

Herein, we encapsulate Pt nanoparticles (NPs) in MOFs to introduce Xe adsorption sites to the MOF to increase its Xe uptake capacity, resulting in enhanced Xe/Kr separation performance (Scheme 1). The Pt NPs were encapsulated in UiO-66 pores (denoted as Pt@UiO-66) using our previously reported one-step method. The resultant Pt@UiO-66 exhibits 21% higher Xe uptake capacity and a 7% increase of Xe/Kr selectivity relative to UiO-66 due to the strong interaction between xenon and the introduced Pt NPs. As a result, Pt@UiO-66 exhibits an 88% increase in breakthrough time in a column breakthrough experiment. Furthermore, we investigated the effect of various contents of Pt NPs on the Xe/Kr separation performance to

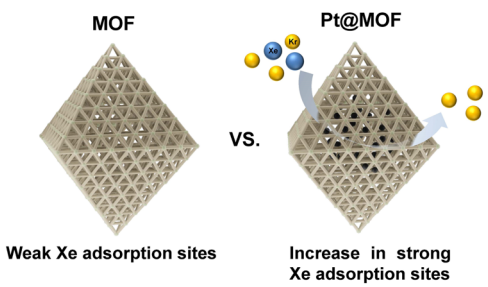

Scheme 1 Encapsulation of Pt NPs with strong Xe adsorption sites in a MOF to enhance Xe/Kr separation.

[a]*Shanghai Institute of Applied Physics, Chinese Academy of Sciences, Shanghai, 201800, China. E-mail: wuchunhui@sinap.ac.cn; chuxinxin@sinap.ac.cn*
[b]*Wuwei Institute of Advanced Energy, Gansu Province, 733099, China*

obtain the optimal Pt NPs loading. When this method was applied to MOF-801, the Xe uptake capacity and Xe/Kr selectivity were also simultaneously enhanced, demonstrating that this method can be potentially applied to different MOFs with excellent Xe/Kr separation performance.

Results and discussion

UiO-66 was selected as the MOF of interest for the study due to its structural robustness and because its pore size can be precisely regulated by ligand modification, making it suitable for molecular sieving separation.[39] Based on our previous work, 2 nm polyvinylpyrrolidone (PVP)-coated Pt NPs were synthesized first (Fig. S1),[40] and were then introduced during the synthesis of UiO-66. Energy dispersive X-ray spectroscopy (EDS) elemental mapping results unambiguously show that the Pt signal from the Pt NPs is evenly distributed in the multi-particle aggregates (Fig. S2). The TEM images further confirm that the Pt NPs are encapsulated in the center of the UiO-66 crystals (Fig. 1A). As shown in Fig. 1A, monodispersed Pt@UiO-66 particles with an average size of ~185 nm were synthesized, which is similar to UiO-66 particles synthesized through the same method without adding Pt NPs (Fig. S3). The scanning electron microscopy (SEM) image showed that Pt@UiO-66 maintained an octahedron morphology with a smooth surface texture, demonstrating that the Pt NPs were only encapsulated inside the UiO-66 crystal (Fig. S4). The powder X-ray diffraction (PXRD) pattern of Pt@UiO-66 was found to be identical to that of the as-synthesized UiO-66, suggesting full retention of the MOF crystallinity after the encapsulation of the Pt NPs (Fig. 1B). Additionally, no characteristic peaks for the Pt NPs were observed in the pattern, which may be due to the low Pt content resulting in weak characteristic peak signals (Fig. S5). The Fourier-transform infrared (FT-IR) analysis showed no considerable differences between the FT-IR spectra of Pt@UiO-66 and UiO-66, suggesting that the functional group features of UiO-66 were fully maintained after the encapsulation of the Pt NPs (Fig. S6). The loading of the Pt NPs was determined to be ~3 wt% using inductively coupled plasma-optical emission spectroscopy (ICP-OES). Furthermore, thermogravimetric analysis (TGA) was performed to investigate the defects of UiO-66 and Pt@UiO-66 (Fig. S7). The Zr/BDC (H_2BDC = benzene-1,4-dicarboxylic acid) ratios of UiO-66 and Pt@UiO-66 were calculated from the TGA curves to be 1.014 and 1.166, respectively. This result indicates that the prepared UiO-66 supports are linker deficient and the encapsulation of Pt NPs increases the defects in UiO-66.

The porosity of Pt@UiO-66 was investigated using N_2 adsorption experiments at 77 K. As shown in Fig. 1C, Pt@UiO-66 exhibits a Brunauer–Emmett–Teller (BET) surface area and pore volume of 1140 $m^2\ g^{-1}$ and 0.440 $cm^3\ g^{-1}$, respectively, which is slightly lower than that of UiO-66 (1240 $m^2\ g^{-1}$ and 0.473 $cm^3\ g^{-1}$). This discrepancy in BET surface area and pore volume is due to the non-porous Pt NPs residues taking up part of the sample weight of UiO-66. Meanwhile, the pore size distribution analysis also confirmed that Pt@UiO-66 exhibited 6–10 Å pores, the same as those found in UiO-66 (Fig. 1D). These results unambiguously demonstrate that the encapsulation of Pt NPs had no negative effect on the MOF porosity.

Next, in order to investigate the Xe and Kr adsorption and separation performance of Pt@UiO-66, single component adsorption isotherm experiments for Xe and Kr were conducted at 298 K. In general, both UiO-66 and Pt@UiO-66 have a higher Xe than Kr uptake capacity (Fig. 2B and C). As shown in Fig. 2C, the Kr uptake capacity of Pt@UiO-66 at 298 K and 1 bar is basically unchanged after encapsulation of the Pt NPs. In contrast, Pt@UiO-66 shows a higher Xe uptake capacity (2.28 mmol g^{-1}) than that of UiO-66 (1.88 mmol g^{-1}), despite

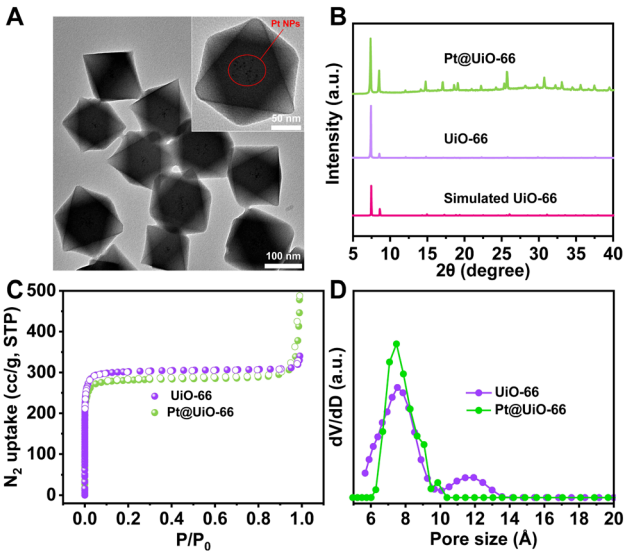

Fig. 1 (A) TEM images of Pt@UiO-66. (B) PXRD patterns of UiO-66 and Pt@UiO-66. (C) N_2 adsorption–desorption isotherms at 77 K of UiO-66 and Pt@UiO-66. (D) Pore size distributions of UiO-66 and Pt@UiO-66.

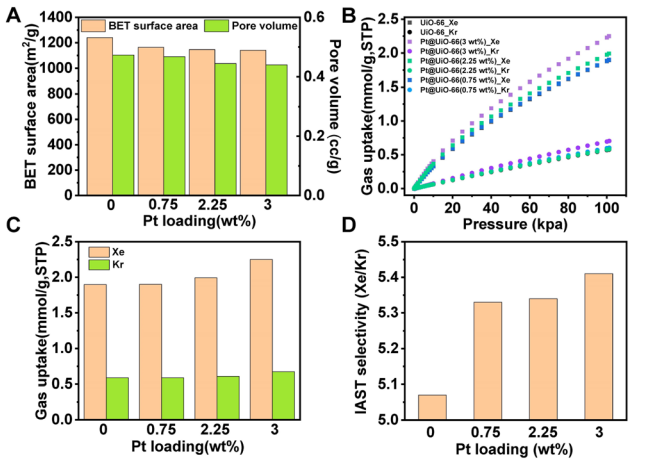

Fig. 2 (A) The BET surface area and pore volume of Pt@UiO-66 with various Pt NP loadings. (B) Kr and Xe adsorption isotherms at 298 K of Pt@UiO-66 with various Pt NP loadings. (C) The Kr and Xe uptake capacity (1 bar, 298 K) of Pt@UiO-66 with various Pt NP loadings. (D) Calculated IAST selectivity at 298 K for a Xe/Kr mixture (v/v = 20/80) of Pt@UiO-66 with various Pt NP loadings.

the BET surface area decreasing. Using the ideal adsorbed solution theory (IAST) (eqn (S2) and Fig. S8),[41] the separation selectivity of a 20 : 80 Xe–Kr binary gas mixture at 298 K and 1 bar was predicted to be 5.41 for Pt@UiO-66, 7% higher than that of UiO-66 (5.07) (Fig. 2D). It is thus reasonable to conclude that the encapsulation of the Pt NPs with strong Xe adsorption sites led to an increased Xe capacity and improved Xe/Kr selectivity.

The isosteric heats of adsorption (Q_{st}) of UiO-66 and Pt@UiO-66 were calculated using the Clausius–Clapeyron equation to evaluate using van't Hoff isochore graphs the interaction between the noble gases and the activated framework (eqn (S4) and Fig. S9). The Q_{st} of Xe for Pt@UiO-66 at low loading was estimated to be 27.4 kJ mol^{-1}, which was higher than that of UiO-66 (24.1 kJ mol^{-1}). The Q_{st} of Kr for Pt@UiO-66 (21.5 kJ mol^{-1}) showed only a slight decrease compared with that of UiO-66 (22.3 kJ mol^{-1}). This result further confirms that Pt@UiO-66 has a stronger binding affinity for Xe than UiO-66.

To further investigate the influence of the Pt loading on the Xe and Kr adsorption and separation performance, Pt@UiO-66 encapsulating different amounts of Pt NPs was prepared through the same method. For simplicity, these samples were denoted as Pt@UiO-66(x) (x represents the Pt loading). As shown in Fig. 2A and S10, with the increase of Pt loading in UiO-66, the BET surface area decreased continuously from 1240 to 1163, 1146 and 1140 m^2 g^{-1} for UiO-66, Pt@UiO-66(0.75), Pt@UiO-66(2.25) and Pt@UiO-66(3), respectively. Meanwhile, the pore volume also decreased from 0.473 to 0.467, 0.444 and 0.440 cm^3 g^{-1}, respectively, due to the encapsulation of the non-porous Pt NPs. In contrast, the Xe uptake capacity at 298 K and 1 bar increased from 1.88 to 1.92, 2.01 and 2.28 mmol g^{-1} for UiO-66, Pt@UiO-66(0.75), Pt@UiO-66(2.25) and Pt@UiO-66(3), respectively, whereas the Kr uptake capacity remained almost constant (Fig. 2B and C). As a result, the Xe/Kr IAST selectivity increased from 5.07 for UiO-66 to 5.33, 5.34 and 5.41 for Pt@UiO-66(0.75), Pt@UiO-66(2.25) and Pt@UiO-66(3), respectively (Fig. 2D). This improvement can be attributed to the introduction of the Pt NPs which interact strongly with Xe. Further increase of the Pt loading to 4 wt% results in the presence of some unencapsulated free Pt NPs (Fig. S11). Hence, Pt@UiO-66(3) was selected as the optimal loading for further research.

Next, to investigate how the introduction of strong Xe adsorption sites affects the dynamic separation performance, a breakthrough experiment was performed in a fixed bed column with a gas mixture composed of 0.1% Xe, 0.4% Kr and 99.5% Ar at 1 atm and 298 K (Fig. S12). The breakthrough curves show that both solid UiO-66 and Pt@UiO-66(3) can effectively separate Xe from Kr due to their strong affinity for Xe over Kr. The total Xe adsorption capacity (q_d) of Pt@UiO-66(3) integrated from the breakthrough curves is 3.554 mmol kg^{-1}, which is higher than that of UiO-66 (1.714 mmol kg^{-1}) (Table S2). As a result, Pt@UiO-66(3) exhibits a Xe breakthrough time (in this work, the breakthrough time (t_b) was arbitrarily defined as the time when C/C_0 reached 1%) of 8.19 min g^{-1}, 88% longer than that of UiO-66 (4.36 min g^{-1}). Meanwhile, the Kr breakthrough time of Pt@UiO-66(3) (0.74 min g^{-1}) is close to that of UiO-66 (0.98 min g^{-1}) (Fig. 3). This suggests that the introduction of strong Xe adsorption sites can enhance the Xe uptake capacity, which subsequently affects the dynamic separation behavior of UiO-66.

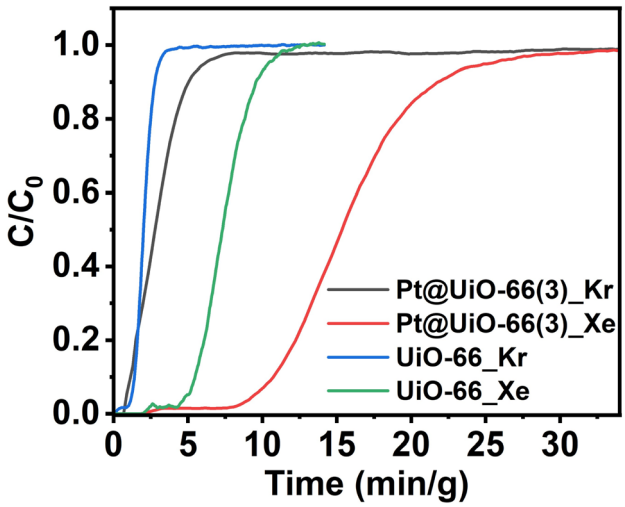

Fig. 3 Column breakthrough curves of UiO-66 and Pt@UiO-66(3) at 1 atm and 298 K using a Kr/Xe/Ar mixture (0.1% Xe, 0.4% Kr and 99.5% Ar).

In order to examine the robustness and regenerability of the developed composite, the column breakthrough curves, adsorption and desorption isotherms of Pt@UiO-66(3) at 298 K were collected after regeneration (Fig. S13). As shown in Fig. S13A, the adsorption and desorption isotherms of Pt@UiO-66(3) before and after regeneration almost overlap after regeneration at 100 °C for 10 minutes under a He flow. Similarly, the total adsorption capacity of Pt@UiO-66(3) (3.391 mmol kg^{-1}) integrated from the breakthrough curves did not decrease significantly compared to the state before regeneration (3.554 mmol kg^{-1}) (Fig. S13B). Pt@UiO-66(3) exhibits Xe and Kr breakthrough times of 8.02 min g^{-1} and 0.71 min g^{-1}, respectively, after regeneration, which remains almost unchanged compared of the initial Pt@UiO-66(3) times (8.19 min g^{-1} and 0.74 min g^{-1}). A fully reversible regeneration was achieved with fast desorption kinetics under mild heating to 100 °C under a He flow. The relatively mild regeneration conditions enable Pt@UiO-66 to be potentially applied in industrial Xe/Kr separation.

Finally, in order to demonstrate the general applicability of this approach to enhance the Xe/Kr separation performance of MOFs by introducing strong Xe adsorption sites, ~3 wt% Pt NPs were encapsulated into MOF-801 by following the same protocol. The transmission electron microscopy (TEM) and SEM images show that the NPs were successfully encapsulated into each MOF-801 particle to give a composite structure, Pt@MOF-801 (Fig. 4A). Synthesized MOF-801 particles were used as a control sample to compare with Pt@MOF-801 (Fig. S14). The PXRD patterns show that the crystallinity of MOF-801 also was fully preserved after the encapsulation of the Pt NPs (Fig. S15). The BET surface area and pore volume of Pt@MOF-801 calculated from the N_2 adsorption isotherms at 77 K were 641.2 m^2

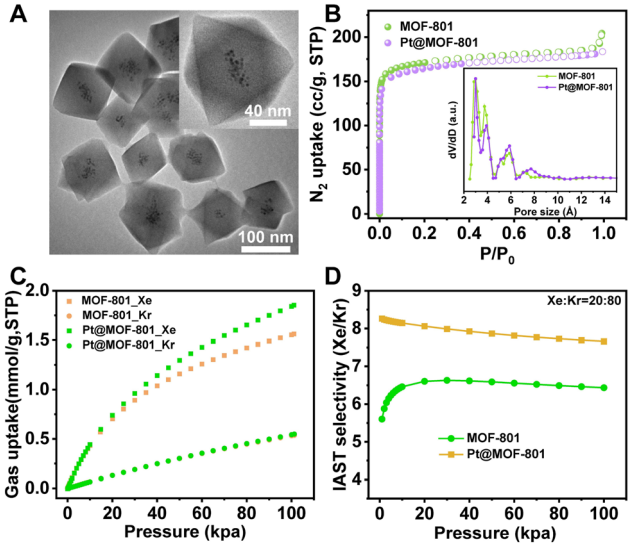

Fig. 4 (A) TEM images of Pt@MOF-801. (B) N_2 adsorption–desorption isotherms at 77 K and pore size distributions of MOF-801 and Pt@MOF-801. (C) Kr and Xe adsorption isotherms at 298 K of MOF-801 and Pt@MOF-801. (D) Calculated IAST selectivity for a Xe/Kr mixture (v/v = 20/80) for MOF-801 and Pt@MOF-801 at 298 K.

g^{-1} and 0.267 $cm^3\ g^{-1}$, respectively. These values are slightly lower than those of MOF-801 (679.6 $m^2\ g^{-1}$ and 0.276 $cm^3\ g^{-1}$) due to the existence of non-porous Pt NPs in the structure (Fig. 4B). The pore size distribution of Pt@MOF-801 is also in good agreement with that of MOF-801 (Fig. 4B). When the Pt@MOF-801 was applied for Xe and Kr adsorption and separation, Pt@MOF-801 shows a similar Kr uptake capacity at 1 bar to that of MOF-801, while the Xe uptake capacity of Pt@MOF-801 (1.85 mmol g^{-1}) is 20% higher than that of MOF-801 (1.56 mmol g^{-1}) (Fig. 4C). As a result, the calculated IAST Xe/Kr selectivity increased from 6.44 for MOF-801 to 7.66 for Pt@MOF-801 (Fig. 4D). This enhancement of Xe uptake capacity and Xe/Kr selectivity follows the same trend as Pt@UiO-66, which demonstrates that this method can be extended to different MOFs to achieve excellent Xe/Kr separation performance.

Conclusions

In summary, a method to enhance the Xe/Kr separation performance of MOFs by introducing NPs into MOFs was developed. The obtained Pt@UiO-66 material exhibited enhanced performance in the adsorption and separation of Xe over Kr. This can be attributed to the introduction of Pt NPs with strong Xe adsorption sites leading to increased Xe uptake capacity and Xe/Kr selectivity. As a result, Pt@UiO-66 manifests a 88% increase in breakthrough time during dynamic Xe/Kr separation. Furthermore, this method can be extended to MOF-801, which also led to enhanced Xe/Kr separation performance, suggesting that this method can be potentially applied to different MOFs, resulting in excellent Xe/Kr separation performance.

Conflicts of interest

There are no conflicts to declare.

Data availability

The data supporting this article have been included as part of the SI.

Supplementary information is available. See DOI: https://doi.org/10.1039/d5ra03389f.

Acknowledgements

This work was sponsored by the Gansu Major Scientific, Technological Special Project (Grant No. 23ZDGH001), the Natural Science Foundation of Gansu Province, China (Grant No. 23JRRH0009), Wuwei Institute of Advanced Energy, the Young Scientists Fund of the National Natural Science Foundation of China (Grant No. 22405288), the Youth Innovation Promotion Association, Chinese Academy of Sciences (Grant No. 2021254) and Shanghai Rising-Star Program (Grant No. 24YF2756300).

Notes and references

1 A. K. Chhandak, R. Israni and A. Trivedi, *Int. J. Curr. Microbiol. Appl. Sci.*, 2017, **6**, 2063–2068.
2 S. C. Cullen and E. G. Gross, *Science*, 1951, **113**, 580–582.
3 G. A. Lane, M. L. Nahrwold, A. R. Tait, M. Taylor-Busch, P. J. Cohen and A. R. Beaudoin, *Science*, 1980, **210**, 899–901.
4 J. Marshall and A. C. Bird, *Br. J. Ophthalmol.*, 1979, **63**, 657–668.
5 P. Chuong and N. Xuan, *Determination of Partial Pressure Ratio of Krypton and Argon in the Mixture of Gases Inserted in Fluorescent Lamps*, National Inst. for Nuclear Research, 1989.
6 G. E. Pavlovskaya, Z. I. Cleveland, K. F. Stupic, R. J. Basaraba and T. Meersmann, *Proc. Natl. Acad. Sci. U. S. A.*, 2005, **102**, 18275–18279.
7 F. G. Kerry, *Industrial Gas Handbook: Gas Separation and Purification*, CRC Press, 2007.
8 S. U. Nandanwar, K. Coldsnow, V. Utgikar, P. Sabharwall and D. E. Aston, *Chem. Eng. J.*, 2016, **306**, 369–381.
9 N. R. Soelberg, T. G. Garn, M. R. Greenhalgh, J. D. Law, R. Jubin, D. M. Strachan and P. K. Thallapally, *Sci. Technol. Nucl. Install.*, 2013, **2013**, 702496.
10 J. P. Fraissard, *Physical Adsorption: Experiment, Theory, and Applications*, Springer Science & Business Media, 1997.
11 C. G. Saxton, A. Kruth, M. Castro, P. A. Wright and R. F. Howe, *Microporous Mesoporous Mater.*, 2010, **129**, 68–73.
12 C. J. Jameson, A. K. Jameson and H.-M. Lim, *J. Chem. Phys.*, 1997, **107**, 4364–4372.
13 R. Bazan, M. Bastos-Neto, A. Moeller, F. Dreisbach and R. Staudt, *Adsorption*, 2011, **17**, 371–383.
14 K. Munakata, T. Fukumatsu, S. Yamatsuki, K. Tanaka and M. Nishikawa, *J. Nucl. Sci. Technol.*, 1999, **36**, 818–829.

15 O. K. Farha and J. T. Hupp, *Acc. Chem. Res.*, 2010, **43**, 1166–1175.
16 O. M. Yaghi, M. O'Keeffe, N. W. Ockwig, H. K. Chae, M. Eddaoudi and J. Kim, *Nature*, 2003, **423**, 705–714.
17 Y.-S. Bae, K. L. Mulfort, H. Frost, P. Ryan, S. Punnathanam, L. J. Broadbelt, J. T. Hupp and R. Q. Snurr, *Langmuir*, 2008, **24**, 8592–8598.
18 K. Sumida, D. L. Rogow, J. A. Mason, T. M. McDonald, E. D. Bloch, Z. R. Herm, T.-H. Bae and J. R. Long, *Chem. Rev.*, 2011, **112**, 724–781.
19 S. M. Cohen, *Chem. Rev.*, 2011, **112**, 970–1000.
20 H.-C. Zhou, J. R. Long and O. M. Yaghi, *Chem. Rev.*, 2012, **112**, 673–674.
21 H. Furukawa, K. E. Cordova, M. O'Keeffe and O. M. Yaghi, *Science*, 2013, **341**, 1230444.
22 S. Kitagawa, *Chem. Soc. Rev.*, 2014, **43**, 5415–5418.
23 G. Maurin, C. Serre, A. Cooper and G. Férey, *Chem. Soc. Rev.*, 2017, **46**, 3104–3107.
24 K. Shao, H. M. Wen, C. C. Liang, X. Xiao, X. W. Gu, B. Chen, G. Qian and B. Li, *Angew. Chem., Int. Ed.*, 2022, **61**, e202211523.
25 J. F. Kurisingal, D. W. Kim and C. S. Hong, *Coord. Chem. Rev.*, 2024, **507**, 22.
26 S. J. Lee, K. C. Kim, T. U. Yoon, M. B. Kim and Y. S. Bae, *Microporous Mesoporous Mater.*, 2016, **236**, 284–291.
27 J. Pei, X.-W. Gu, C.-C. Liang, B. Chen, B. Li and G. Qian, *J. Am. Chem. Soc.*, 2022, **144**, 3200–3209.
28 X. L. Wu, Z. J. Li, H. Zhou, G. Yang and W. Liu, *Inorg. Chem.*, 2021, **60**, 1506–1512.
29 Y. Yang, C. Tu, L. Guo, L. Wang, F. Cheng and F. Luo, *Cell Rep. Phys. Sci.*, 2023, **4**, 101694.
30 H. Zhang, Y. Fan, R. Krishna, X. Feng and F. Luo, *Sci. Bull.*, 2020, **66**, 1073–1079.
31 X. Wang, F. Ma, S. Xiong, Z. Bai, Y. Zhang, G. Li, J. Chen, M. Yuan, Y. Wang and X. Dai, *ACS Appl. Mater. Interfaces*, 2022, **14**, 22233–22241.
32 M. Dixit, T. Adit Maark, K. Ghatak, R. Ahuja and S. Pal, *J. Phys. Chem. Sci.*, 2012, **116**, 17336–17342.
33 J. Liu, D. M. Strachan and P. K. Thallapally, *Chem. Commun.*, 2014, **50**, 466–468.
34 C. Daniel, A. Elbaraoui, S. Aguado, M.-A. Springuel-Huet, A. Nossov, J.-P. Fontaine, S. Topin, T. Taffary, L. Deliere and Y. Schuurman, *J. Phys. Chem. C*, 2013, **117**, 15122–15129.
35 L. Deliere, B. Coasne, S. Topin, C. Gréau, C. Moulin and D. Farrusseng, *Chem.–Eur. J.*, 2016, **22**, 9660–9666.
36 X. Gu, Z.-H. Lu, H.-L. Jiang, T. Akita and Q. Xu, *J. Am. Chem. Soc.*, 2011, **133**, 11822–11825.
37 A. Monpezat, J. Aupiais and B. Siberchicot, *ACS Omega*, 2021, **6**, 31513–31519.
38 D.-L. Chen, W. Al-Saidi and J. K. Johnson, *J. Phys.: Condens. Matter*, 2012, **24**, 424211.
39 J. H. Cavka, S. Jakobsen, U. Olsbye, N. Guillou, C. Lamberti, S. Bordiga and K. P. Lillerud, *J. Am. Chem. Soc.*, 2008, **130**, 13850–13851.
40 C. Wu, X. Zhao, D. Wang, X. Si and T. Li, *Chem. Sci.*, 2022, **13**, 13338–13346.
41 A. L. Myers and J. M. Prausnitz, *AIChE J.*, 1965, **11**, 121–127.